Prediction of energy dissipation in violent sloshing flows simulated by Smoothed Particle Hydrodynamics

S. Marrone, A. Colagrossi
CRN-INM
Institute of Marine Engineering
Rome, Italy
salvatore.marrone@cnr.it

L. González-Gutiérrez, J. Calderon-Sanchez, J. Martinez-Carrascal
School of Naval Engineering
Universidad Politécnica de Madrid
Avda. de la Memoria 4 28040 Madrid Spain

Abstract—**The present work aims to investigate the use of fuel sloshing to reduce the design loads on aircraft wings. These are highly flexible structures, that can deform significantly under certain loading. Wings house the fuel tanks, and generally carry an amount of fuel comparable in weight to that of their structural components. In the present research the SPH model is adopted to investigate the damping effect of fuel sloshing on the dynamics of flexible wing-like structures. This represents a quite challenging task for SPH and more in general, for CFD tools, being the fuel tank under study subjected to vertical accelerations as high as 10g. The resulting flow is extremely complex due to the highly turbulent flow, the violent impacts and intense fragmentation of the air-liquid interface. The straightforward application of SPH to the problem suffers from some numerical issues, such as the tensile instability. To this aim the recent δ-LES-SPH model is adopted. The focus of the analysis is on the energy balance of the mechanical system. In particular, the experiments in [14] are reproduced in the numerical simulations comparing the flow evolution and the obtained forces and dissipated energy.**

I. Introduction

There are an important number of situations involving a liquid that evolves dynamically in a confined portion of space. These situations can be found either when the liquid, typically a kind of fuel, is transported from different (air)ports or when it is used as Tuned Liquid Damper (TLD) to counteract the motions caused by an external agent, such as building motion during earthquakes, ship rolling motion due to waves or any other complex dynamic phenomena. All the situations that have been described imply that the confined liquid moves inside the tank with high accelerations and strong wall impacts, and are commonly identified as examples of sloshing flows. Lately, a typical and attractive example of this kind of confined flow is found in the kerosene containers placed within aircraft wings, where the fluid is moved by violent structural loads coming in turn from external wind gusts and air turbulence. In this application, the fluid is vertically accelerated up to typical values in the order of $10g$, which results in amplitudes comparable to the tank dimensions and frequencies higher than 5 Hz.

In this context several experiments, such as the ones conducted by [14], have demonstrated that fluid motion plays a role on the wing structure, acting as a damper. In these conditions the initial stages of the flow evolution are driven by intense breaking of the free surface due to the impulsive heaving motion of the tank, also inducing a detachment of the fluid from the tank walls. The previous flow regime is somehow different to what is normally described as a "sloshing flow", as the fluid is continuously violently slamming alternately upward and downward against the top and bottom walls, whilst in the common literature the term "sloshing flow" is used to describe those situations when the tank accelerations are smaller than 2-3g, and the flow is essentially driven by gravity forces.

Recently, a thorough validation on sloshing flows occurring in tanks of different shapes has been carried out by [8], [9]. The SPH method can be regarded as an efficient methodology when compared to mesh-based methods to simulate free surface flows, and precisely those including violent sloshing (see *e.g.*, [5], [10]). In order to accurate simulate the considered violent flows important particular aspects of the classical SPH method have to be addressed: to limit the "tensile instability" onset, a particle shifting technique, as the one reported by [18] can be adopted. The latter allows, at the same time, the achievement of making accurate computations with little spurious energy dissipation by enforcing uniform particle distributions; further, assuming that the flow is highly turbulent and that multiple scales are involved in the fluid diffusion process, only the largest scales are included in the simulation due to the limited computational capacity. The sub-grid scales are here included using a Large Eddy Simulation (LES) model such as the δ-LES-SPH described in [3], [7]. The latter allows also for an accurate evaluation of pressure fields thanks to the presence of diffusive terms in the mass conservation equation as in the δ-SPH formulation.
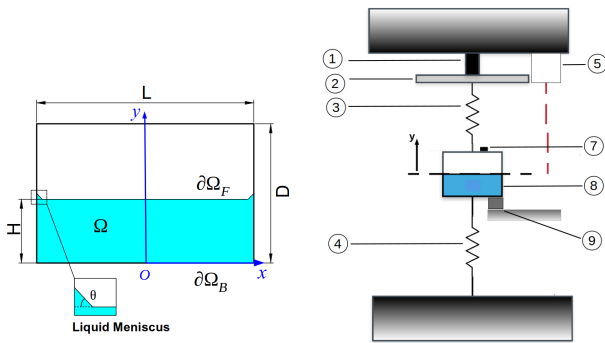
Fig. 1. Left plot: sketch of the numerical domain. Right plot: Outline of the experimental setup.

II. Problem description

In [14] a violent sloshing flow in a vertically moving tank with a single degree of freedom has been experimentally studied. In the present work the conditions adopted in that experimental campaign are considered for the numerical simulations. In [14] a tank with geometry 10x6x6 cm is connected to a set of 6 springs, 3 on the upper side and 3 on the lower side. The tank is filled up to 50 % of its volume with a water mass of $m_l = 0.18$ kg and, when the springs are released, oscillates at a characteristic frequency of $f_0 = 6.51$ Hz.

An outline of the experimental setup at the Model Basin Research group sloshing laboratory of the UPM is shown in right plot of figure 1. The experimental rig is composed of a mechanical guide that allows the single degree of freedom constraint. In the left plot of figure 1 a schematic representation of fluid domain is reported. The acceleration and position of the tank as well as load cell measurements are recorded allowing the calculation of the sloshing force acting on the system. A more detailed description of the experimental setup and vertical sloshing force derivation can be found in [14].

In figure 2 it can be seen that the flow is divided into four main stages. First, right after the release at $t = 0.058$ s the liquid menisci, formed at the intersection between the liquid interface and the solid wall, start travelling toward the tank centre forming a ripple at the free surface that triggers a vertical Rayleigh-Taylor instability. The instability travels in the upward direction and causes the first impact against the ceiling at $t = 0.083$ s. After that, the free surface is fragmented and the flow can be considered as highly turbulent, characterized by many fluid-fluid and fluid-wall impacts (see plot at $t = 1.22$). Finally, when the tank motion is attenuated, at around $t = 2.4$ s the last fluid-wall impact happens and a standing wave regime develops until the system reaches the rest condition. From this experimental study, the vertical sloshing force, tank acceleration and position are obtained. These results are used in Section VI to validate the numerical outcomes.

III. Governing equations

In the present work a two-dimensional fluid domain Ω delimited by a free surface $\partial\Omega_F$ and closed solid surface $\partial\Omega_B$ is considered (see left plot of Fig. 1). The domain Ω contains only a liquid phase and $\partial\Omega_B$ represents the internal surface of a moving tank. The governing equations adopted are the Navier-Stokes equations (NSE) for a single-phase weakly-compressible fluid. These can be either solved in an Inertial Frame of Reference (I-FoR) where the tank is moving, or in a Non-inertial Frame of Reference (Ni-FoR) moving with tank motion. In the latter case the non-inertial accelerations f_{NI} due to the tank motion need to be added to the momentum equation. While the use of I-FoR or Ni-FoR does not affect the evaluation of the energy dissipated by the liquid motions, the numerical procedures can be affected by this choice. Due to its easier implementation the Ni-FoR is generally preferred, and also because it avoids numerical errors related to the tank motion. This is, indeed, the choice made in the present work.

Since a weakly-compressible regime is assumed, a simple linear equation of state can be adopted:

$$p = c_0^2 (\rho - \rho_0), \tag{1}$$

where c_0 is the speed of sound (assumed constant) of the liquid medium and ρ_0 the density at the free-surface (where p is assumed to be equal to zero).

The main simplifications adopted in the numerical model to reproduce the experiment are:

- a two-dimensional framework;
- the air phase is neglected (only the liquid phase is modelled);
- thermal conductivity and surface tension effects are neglected;
- weakly-compressible regime is always attained using an artificial speed of sound.

Although the first two may be regarded as strong approximations for modelling violent sloshing flows, we will show that it is possible to obtain a fair estimation of the dissipated energy when comparing the numerical outputs against experimental measurements. It is worth noting that in [11] it is shown that when modelling breaking waves the differences between 2D and 3D frameworks are generally small, the difference of the dissipated energy being smaller than 10% even after a few wave periods from the first breaking event. Regarding the use of a single-phase model and neglecting the role of the air contained in Ω, in [13] it was shown that the evaluation of the energy dissipation in violent flows even within this hypothesis can be still accurate enough. On the other hand, this does not mean that the role of the air phase cannot play a relevant role on fluid dynamics, especially in terms of local pressure and velocity fields. Furthermore, in simulations involving water, the adopted spatial resolution is not sufficient to resolve the Wall Boundary Layer (WBL) regions and, for this reason, the free-slip conditions are used. Conversely, for simulations involving oil, due to the lower Reynolds number

$$t = 0.055 \text{ s} \qquad t = 0.083 \text{ s} \qquad t = 1.22 \text{ s} \qquad t = 2.4 \text{ s}$$
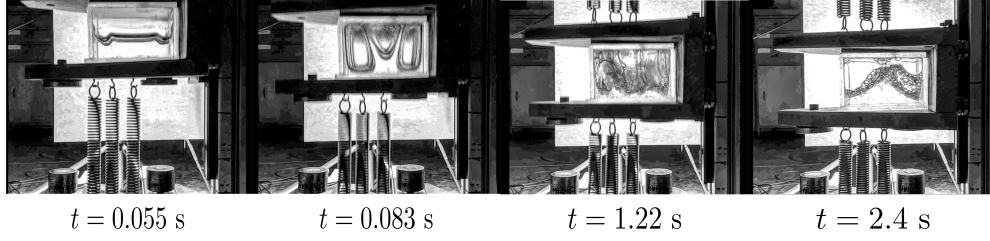
Fig. 2. Experimental snapshots of the SDOF vertical sloshing water experiments carried out in [14] for vertical acceleration equal to $10g$ and frequency oscillation equal to 6.51 Hz.

it is possible to resolve the WBL regions, and therefore, for these simulations the no-slip conditions are used.

IV. BRIEF RECALL OF THE δ-LES-SPH MODEL

Because of the high Reynolds number related to the experiments described in the previous section, in the numerical scheme a sub-grid model for the turbulent viscosity is needed. To this end the δ-LES-SPH model described [3], [15] is considered, where a LES modeling is rewritten in a Lagrangian formalism and introduced in the SPH system of equations:

$$\begin{cases} \dfrac{\mathrm{d}\rho_i}{\mathrm{d}t} & = -\rho_i \sum_j (\boldsymbol{u}_{ji} + \delta\boldsymbol{u}_{ji}) \cdot \nabla_i W_{ij} V_j + \\ & \quad + \sum_j (\rho_j \delta\boldsymbol{u}_j + \rho_i \delta\boldsymbol{u}_i) \cdot \nabla_i W_{ij} V_j + \mathcal{D}_i^\rho \\[2mm] \rho_i \dfrac{\mathrm{d}\boldsymbol{u}_i}{\mathrm{d}t} & = -\sum_j (p_j + p_i)\nabla_i W_{ij} V_j + m_i \boldsymbol{g} + \\ & \quad + \rho_0 \sum_j (\boldsymbol{u}_j \otimes \delta\boldsymbol{u}_j + \boldsymbol{u}_i \otimes \delta\boldsymbol{u}_i) \cdot \nabla_i W_{ij} V_j + \boldsymbol{F}_i^v \\[2mm] \dfrac{\mathrm{d}\boldsymbol{r}_i}{\mathrm{d}t} & = \boldsymbol{u}_i + \delta\boldsymbol{u}_i, \quad V_i = m_i/\rho_i, \quad p = c_0^2(\rho - \rho_0), \end{cases}$$
(2)

where $\boldsymbol{F}_i^v$ are the viscous forces acting on the particle i, while $\delta\boldsymbol{u}$ is the Particle Shifting velocity adopted to regularize the particles' spatial distribution during their motion. The particle masses m_i are assumed to be constant during their motion. As in [3] a C2-Wendland kernel is adopted in the present work. The above equations are written in an Arbitrary-Lagrangian-Eulerian framework. For this reason the continuity and the momentum equations contain terms with spatial derivatives of $\delta\boldsymbol{u}$ (for details see [4]). The notation $\boldsymbol{u}_{ji}$ in (2) indicates the differences $(\boldsymbol{u}_j - \boldsymbol{u}_i)$ and the same holds for $\delta\boldsymbol{u}_{ji}$ and $\boldsymbol{r}_{ji}$.

The term $\mathcal{D}_i^\rho$ is the numerical diffusive term introduced by [1] to filter out the spurious high-frequency noise in the pressure field. Following [3] this term is rewritten within an LES framework as follow:

$$\begin{cases} \mathcal{D}_i^\rho & := \sum_j \delta_{ij} \boldsymbol{\psi}_{ji} \cdot \nabla_i W_{ij} V_j, \\[2mm] \boldsymbol{\psi}_{ji} & := \left[(\rho_j - \rho_i) - \dfrac{1}{2}\left(\langle\nabla\rho\rangle_i^L + \langle\nabla\rho\rangle_j^L \right) \cdot \boldsymbol{r}_{ji} \right] \dfrac{\boldsymbol{r}_{ji}}{\|\boldsymbol{r}_{ji}\|^2} \\[2mm] \delta_{ij} & := 2 \dfrac{\nu_i^\delta \nu_j^\delta}{\nu_i^\delta + \nu_j^\delta}, \qquad \nu_i^\delta := (C_\delta l)^2 \|\mathbb{D}_i\| \end{cases}$$
(3)

where C_δ is a dimensionless constant set equal to 6 while $l = 4\Delta r$ is the support of the kernel W, Δr being the particle size, and represents the length scale of the filter adopted for the sub-grid model. $\|\mathbb{D}\|$ is a rescaled Frobenius norm, namely $\|\mathbb{D}\| = \sqrt{2\mathbb{D} : \mathbb{D}}$. The superscript L in (3) indicates that the gradient is evaluated through gradient renormalization where $\mathbb{L}_i$ is the renormalization matrix.

The viscous forces $\boldsymbol{F}^v$ are expressed as:

$$\begin{cases} \boldsymbol{F}_i^v & := K \sum_j (\mu + \mu_{ij}^T) \pi_{ij} \nabla_i W_{ij} V_j, \qquad \pi_{ij} := \dfrac{\boldsymbol{u}_{ij} \cdot \boldsymbol{r}_{ij}}{\|\boldsymbol{r}_{ji}\|^2} \\[2mm] \mu_{ij}^T & := 2 \dfrac{\mu_i^T \mu_j^T}{\mu_i^T + \mu_j^T}, \qquad \mu_i^T := \rho_0 (C_S l)^2 \|\mathbb{D}_i\| \end{cases}$$
(4)

where $K = 2(n+2)$, n being the number of spatial dimensions, and C_S is the so called Smagorinsky constant set equal to 0.18 (see [17]). The viscous term (4) contains both the effect of the laminar viscosity μ as well as the one related to the local turbulent viscosity μ_i^T. Finally, the Particle Shifting velocity $\delta\boldsymbol{u}$ is defined as in [18]. As documented in [18], the use of the Particle Shifting Technique (PST) leads to regular particle distributions. In turn, the inclusion of the PST causes the loss of the exact conservation of the angular momenta as commented in [18].

V. ENERGY DISSIPATION WITHIN THE δ-LES-SPH MODEL

Following the analysis performed in [2] and in [15] the energy balance for the particle system can be extended to the δ-LES-SPH equation presented in the previous section. For the sake of brevity only the main terms are briefly reported in this section. The δ-LES-SPH energy balance can be written as:

$$\dot{\mathcal{E}}_M + \dot{\mathcal{E}}_C = \mathcal{P}_V + \mathcal{P}_V^{turb} + \mathcal{P}_N + \mathcal{P}_{ext}, \quad \mathcal{P}_N := \mathcal{P}_\delta + \mathcal{P}(\delta\boldsymbol{u})$$
(5)

where $\mathcal{E}_M$ is the mechanical energy of the particle system, composed of kinetic energy $\mathcal{E}_K = \frac{1}{2}\sum_i m_i \|\boldsymbol{u}_i\|^2$ and potential energy $\mathcal{E}_P = \sum_i m_i g y_i$ whereas $\mathcal{E}_C$ is the elastic potential energy associated with the fluid compressibility (see, e.g., [12]). The external power $\mathcal{P}_{ext}$ due to the tank motion is evaluated through the mutual interaction between fluid and

solid particles, as detailed in [2] and [6]. Following the latter, the power related to the viscous forces is given by:

$$
\begin{cases}
\mathcal{P}_V &= \mu \dfrac{K}{2} \sum_i \sum_j \pi_{ij} \boldsymbol{u}_{ij} \cdot \nabla_i W_{ij} V_i V_j, \\
\mathcal{P}_V^{turb} &= \dfrac{K}{2} \sum_i \sum_j \mu_{ij}^T \pi_{ij} \boldsymbol{u}_{ij} \cdot \nabla_i W_{ij} V_i V_j
\end{cases}
\tag{6}
$$

Finally, the term $\mathcal{P}_N$ takes into account the effect of the density diffusion $\mathcal{P}_\delta$ (see [15]):

$$
\mathcal{P}_\delta = \sum_i \frac{p_i}{\rho_i} \sum_j \delta_{ij} \boldsymbol{\psi}_{ij} \cdot \nabla_i W_{ij} V_i V_j,
\tag{7}
$$

and the term related to the particles shifting $\delta \boldsymbol{u}$, i.e $\mathcal{P}(\delta \boldsymbol{u})$. Both these two terms are related to the stability of the scheme and are collected together in $\mathcal{P}_N$ as a numerical diffusive term. The energy dissipated in the numerical scheme, $\mathcal{E}_{diss}$, can be directly evaluated as::

$$
\mathcal{E}_{diss} = \int_{t_0}^t \mathcal{P}_{diss}\, dt, \qquad \mathcal{P}_{diss} := \mathcal{P}_V + \mathcal{P}_V^{turb} + \mathcal{P}_N.
\tag{8}
$$

As discussed in [12], during liquid impacts energy losses occur. The weakly-compressible assumption underlying our scheme implies that during impacts, a portion of the mechanical energy is converted into internal compressible energy in the form of acoustic waves, and then is mainly dissipated by numerical diffusive terms, i.e. the $\mathcal{P}_\delta$ term. Therefore, as shown in [15], the energy lost in liquid impacts is represented by the $\mathcal{P}_N$ component. That numerical dissipation, however, becomes less important with respect to viscous dissipation ($\mathcal{P}_V + \mathcal{P}_V^{turb}$) when impacts are not occurring and vortical structures are generated during the post-impact events. When increasing the spatial resolution both $\mathcal{P}_N$ and $\mathcal{P}_V^{turb}$ decrease while the real viscosity component $\mathcal{P}_V$ increases, as more and more small scales of the velocity gradient (i.e. shock waves and small vortexes) are resolved.

VI. RESULTS: SLOSHING IN FORCED DECAY HEAVE MOTION

In this section the experiment described in Section II is addressed. The problem is studied following two steps of increasing complexity.

- Test N.1: the acceleration time history recorded in the experiments in [14] is applied to the tank. In this case it is possible to compare the forces and the external work done on the fluid.
- Test N.2: the complete coupled Fluid Structure Interaction (FSI) problem is considered. The observed numerical tank displacements are compared to the experimental ones.

For all the test cases the tank height is D=0.06 m, the width is L=0.1 m and the tank filling level is 50%, that is, the water depth is H=0.03 m. In the experiment, when the fluid is at rest, a meniscus is formed close to the vertical walls because of the surface tension. This is numerically replicated in the initial conditions by adding, close to the vertical boundaries, a small fluid triangle of the same angle and height as in the experiment (left plot of figure 1), respectively $\theta = 45°$ and
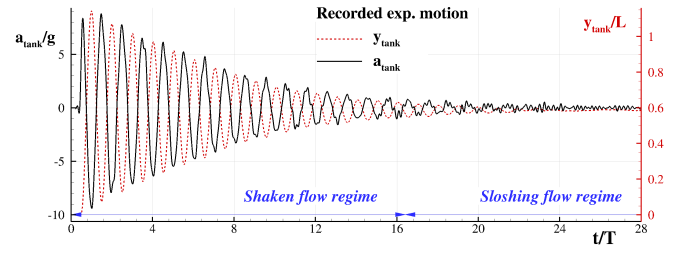
Fig. 3. Tank motion recorded in the experiment of [14] plotted in terms of elevation (dashed line) and acceleration of the tank (solid line).

$l = 1.5\, mm$. The speed of sound adopted in all the simulations $c_0 = 40\, m/s$.

A. Test N. 1: Sloshing in forced motion: experimental damped motion law

In this section the law of motion resulting from the experiment in [14] is imposed on the tank. The maximum amplitude of the oscillation motion, taken from recordings in the experiment, is $2A/L = 1.14$. The frequency of motion is defined as $f_0 = 6.51$ Hz and the period $T = 1/f_0 = 0.154 s$ will be used as a characteristic time scale. We can define the characteristic velocity to be $U_{max} = 2\pi A/T = 2.33$ m/s. The corresponding Reynolds number depends on the fluid tested. The reference case used in this work corresponds to water, with Re$= \rho U L/\mu = 233,000$, with dynamic viscosity $\mu = 0.001\, Pa \cdot s$. Throughout the session the dissipated energy, $\mathcal{E}_{diss}$, is made non-dimensional by the potential energy $\Delta \mathcal{E} = \rho L H g 2A = 3.355$ J, unless otherwise specified.

In figure 3 the recorded motion of the tank is plotted in terms of elevation and acceleration of the tank. In the same figure the portion of the time evolution for which the flow is in the "shaken flow" regime is highlighted. We define here the "sloshing" regime as starting when $a_{tank}/g \leq 1$, a_{tank} being the tank acceleration. In figure 4 the energy decay obtained by the SPH simulation is reported along with the tank displacement. The adopted resolution is $N = H/\Delta x = 400$. A stepped shape of the energy curve can be recognised in the first 10 periods of oscillation, each step corresponding to a liquid impact against the ceiling or the floor of the tank. This energy loss is mostly due to the generation of acoustic waves at the contact line between the free surface and the wall (with dissipation mechanisms similar to those described in [12]) and to the generation of high vorticity due to multiple reconnections of the fluid jets. The rate of dissipated energy then decreases in time and becomes very small when the shaken flow regime is ended and the sloshing regime takes place. In the same figure 4, some relevant instants of the flow are labelled. Labels a) to d) are reported in figure 5, in terms of free-surface configuration and contour of the turbulent viscosity ratio μ_T/μ. Regions of the flow where μ_T/μ is higher are representative of a higher level of local energy dissipation.

In the initial stage, during the first upward acceleration of the tank, a small free-surface wave is generated due to
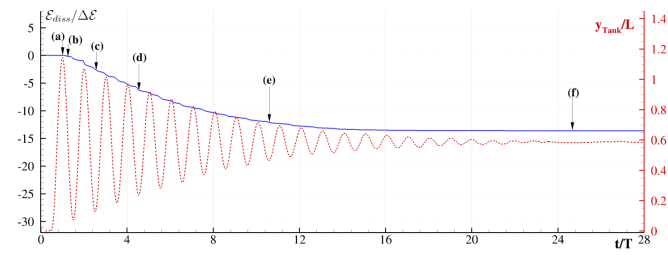
Fig. 4. Time history of the energy decay obtained by the SPH simulation at $N = 400$ (blu solid line). The dashed line represents the tank elevation. Labels (a) to (f) correspond to the same time instants of figure 5 and 6.

Fig. 5. Four representative instants of the flow evolution obtained by the SPH simulation at $N = 400$ for the Re=233,000 case. Contours refer to turbulent viscosity ratio μ_T/μ.

Fig. 6. SPH simulation at $N = 400$ for the Re=233,000 case: vorticity contour at $t/T = 10.54$ (left plot) and $t/T = 24.64$ (right plot).

the rupturing of the menisci at the lateral walls. The waves travel from the lateral walls towards the center of the tank. At $t/T = 0.75$, when the acceleration changes sign, those small free-surface perturbations become the triggering points from which the Rayleigh-Taylor instability develops (plot (a) of 5). The fluid is accelerated upwards and two main jets detach from the free-surface, eventually impacting against the tank ceiling. The flow evolution does not imply any relevant loss of the mechanical energy until the impact at $t/T \simeq 1.26$ (plot (b)): small jets on the sides are generated and high velocity gradients occur in the center where the two main jets collide; this stage is associated to large energy dissipation. Then, the fluid starts a series of cyclical impacts against the top and the bottom of the tank as in (c) and (d), in which two impacts at the tank bottom are shown: the fluid is mostly fragmented in multiple jets and the energy is mainly dissipated in free-surface re-connections and the consequent generation of vorticity. In figure 6, the flow evolution at the time instants related to labels (e) and (f) of figure 4 is shown in terms of vorticity contours. These two time instants are representative of the transition from the "shaken" flow regime to the "sloshing flow" regime: in plot e) the flow is still highly fragmented with production of vorticity distributed on a wide range of length scales; in f) the vorticity intensity is strongly reduced and no roof impacts occur anymore: the fluid appears compact with very small local breakings and a large gravity wave travels on the liquid surface. This is the typical behaviour of moderate sloshing flows.

In order to better understand the energy dissipation mechanisms acting in the δ-LES-SPH, in the left plot of figure 7 the different energy components presented in eq. (8) are reported. The turbulent viscous dissipation $\mathcal{E}_V^{turb}$ is the most prominent term among the others, and after 25 periods of oscillation, contributes to 67% of the total energy dissipation. The numerical term, $\mathcal{E}_N$, is the second one contributing to 37% and is essentially related to the strong shock waves generated during liquid collisions. As for the resolved viscous dissipation, this term amounts to about 8% of the total dissipation.This means that the spatial discretization should be further increased in order to have a proper LES modeling of the flow.

In order to investigate the numerical convergence for this problem, three spatial resolutions have been considered,
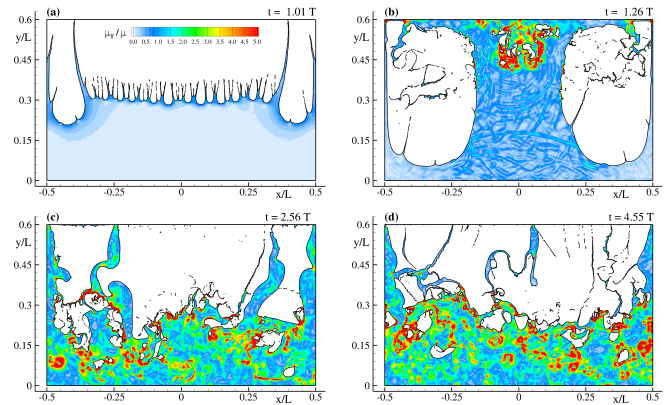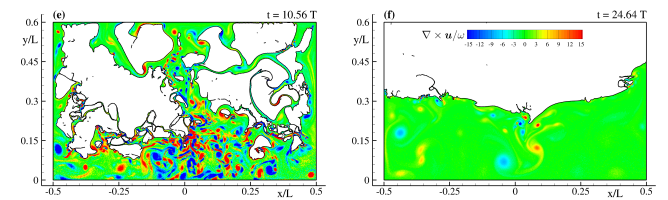
namely $N = H/\Delta x = 50, 100$ and 200; for each discretization 10 repetitions of the same simulation have been performed applying a noise of $0.01\Delta r$ on the initial lattice. Indeed, due to the complexity and high Reynolds of the flow, each simulation has a low repeatability and therefore an averaging over several realizations is needed to obtain reliable results. The result of this study is summarized in the right plot of figure 7. Each curve represents the ensemble average of the 10 repetitions of the same simulation and the error bars indicate the standard deviation. Due to the large computational costs involved, the simulation with the highest resolution, $N = 400$, was not included in this study. The numerical solution exhibits a convergence in terms of average curves. The convergence is on the order of about 1.5. However, the standard deviation does not decrease with the increasing resolution. A possible reason is related to the limited time history of the simulation. In fact, in the short time range the variability becomes prominent due to the rapidly decaying motion.

In order to better investigate the role of viscous effects, the same simulation has been conducted by drastically reducing the simulation Reynolds number. To this end, the considered liquid has been changed to oil, which has kinematic viscosity of $5 \cdot 10^{-5} m^2/s$ corresponding to Re=4,660 (oil density $\rho = 900\,kg/m^3$, dynamic viscosity $\mu = 4.5 \cdot 10^{-2}\,Pa \cdot s$). In this case the energy terms are made non-dimensional through the potential energy $\Delta\mathcal{E} = \rho LHg2A = 3.020$ J. The spatial resolution is again $N = 400$. As mentioned in Section III, for
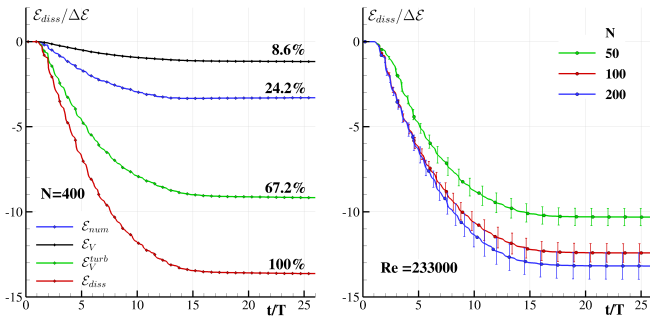
Fig. 7. Left: time history of the energy components defined in Section III: laminar viscous dissipation $\mathcal{E}_V$, turbulent viscous dissipation $\mathcal{E}_V^{turb}$, numerical diffusion $\mathcal{E}_N$, total energy dissipation $\mathcal{E}_{diss}$ for the case N400 and Re=233,000. Right: ensemble average of of the energy dissipation $\mathcal{E}_{diss}$ time history for resolutions $N = 50$, $N = 100$, $N = 200$; error bars refer to the computed standard deviation.
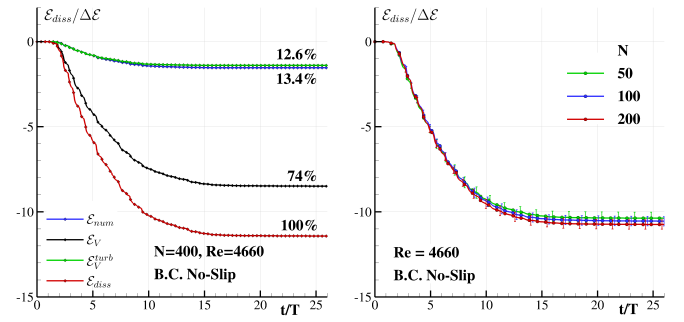
Fig. 9. Left: time history of the energy components defined in section III: laminar viscous dissipation $\mathcal{E}_V$, turbulent viscous dissipation $\mathcal{E}_V^{turb}$, numerical diffusion $\mathcal{E}_N$, total energy dissipation $\mathcal{E}_{diss}$ for the case N400 and Re=4,660. Right: ensemble average of of the energy dissipation $\mathcal{E}_{diss}$ time history for resolutions $N = 50$, $N = 100$, $N = 200$; error bars refer to the computed standard deviation.
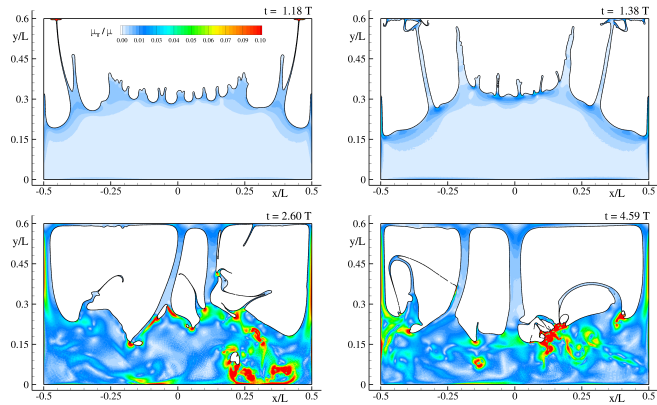
Fig. 8. Four representative instants of the flow evolution obtained by the SPH simulation at $N = 400$ for the Re=4,660 case. Contours refer to turbulent viscosity ratio μ_T/μ.

this simulation no-slip wall boundary conditions are used due to the relevance of boundary layers for this test case. Indeed, using the Blasius theory the thickness δ_{BL} of the wall boundary layer for this case is estimated to be $H/\delta_{BL} = O(10^2)$ which can be adequately resolved with the adopted spatial discretization.

In figure 8 the flow evolution for the same time instants as in figure 4 is reported. Due to the greater viscosity, the liquid does not truly impact against the roof in the first cycle of the tank motion: only two thin jets go to the ceiling at $t = 1.18T$, but the bulk of the flow has not got enough kinetic energy to reach it when the tank acceleration inverts its motion (top-right plot of figure 8). Notwithstanding, the small jets are energetic enough to disrupt the compact shape of the fluid when they fall back down, generating large vortical structures. In the bottom plots of figure 8 the contour plots of the ratio μ_T/μ are shown for two bottom impacts corresponding to labels c) and d) of figure 4. In this case the highest values attain $\mu_T/\mu = 0.1$, showing that the solution is now close to a DNS.

In the left plot of figure 9 the components of the dissipated energy are reported. The most prominent energy component in this case is represented by the laminar viscous term $\mathcal{P}_V$, which

at the end of the simulation amounts to 74% of the total dissipation. The numerical dissipation $\mathcal{E}_N$ is almost halved with respect to the case with water whereas the turbulent viscous energy dissipation is dramatically reduced. This reflects the fact that at this Re a large portion of the viscous dissipation is resolved and the remaining amount of residual energy is dissipated during impacts by means of the power terms $\mathcal{P}_N$ and $\mathcal{P}_V^{turb}$.

Also for this test case the convergence study (right plot of figure 9) has been performed in terms of ensemble average of the energy time history. Distinct from the water case, here it is clear that the average solution does not depend significantly on the spatial resolution. This fact suggests that the adopted LES filter lies well below the inertial range for all the adopted discretizations [16], and therefore, even for the coarsest resolution the obtained solution is an acceptable representation of the large eddies developed in the flow. Further, the standard deviation is largely reduced, which is an expected behaviour for this lower regime of Reynolds number, contributing to decreasing the uncertainty of the obtained solution.

In top plot of figure 10 the vertical forces obtained for resolutions $N = 50, 100$ and 200 are reported in terms of average ensemble over the 10 repetitions performed for each spatial resolution. Remarkably, only small discrepancies are observed between the different resolutions. This is to be ascribed to the inertial forces which account for a large part of the total force. In bottom plot of figure 10 the computed force at $N = 400$ is compared to the experimental observation. Note that experimental data are filtered through a 4th order Butterworth filter with a cutoff frequency of $f_{cut} = 7.7f_0 = 50$ Hz (see [14]) The numerical outcome is, generally, in good agreement with the experiment, especially if one considers the different approximations inherent in the adopted numerical model. In the initial stage of the simulation, around $t/T = 1$, a large discrepancy is observed. At this stage, in the numerical simulation the flow has not impacted yet against the roof (see figure label (a) of 5). Therefore, this could be due to a non-perfect action of the release mechanism in the experiment, or
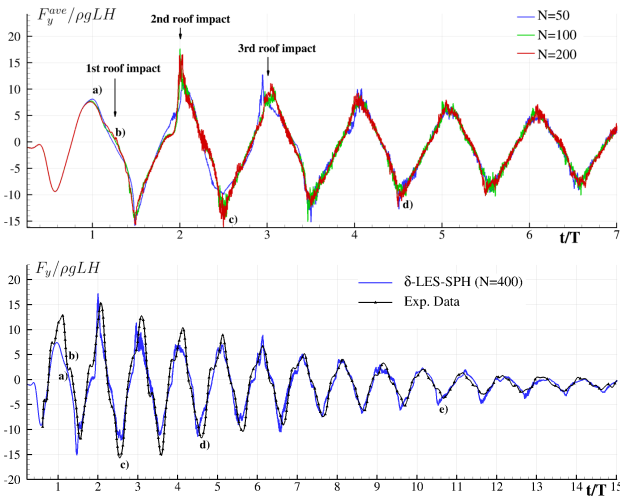
Fig. 10. Top plot: ensemble average of the total vertical force for resolutions $N = 50$, $N = 100$, $N = 200$ for water simulations. Bottom plot: force comparison between the experimental data for the water case and the SPH simulation at N=400.

Fig. 11. Top plot: Time history of the the external work $\mathcal{W}_{ext}^{dyn}$ computed in the simulation and evaluated in the experiment for the water case. Bottom plot: same quantities for the oil case.

to differences in the initial flow deformation.

In figure 11 the work done by hydrodynamic forces, defined as:

$$\mathcal{W}_{ext}^{dyn} := \int_{t_0}^{t} v_{tank} \, \boldsymbol{j} \cdot [\boldsymbol{F}_y - M_{liquid} \, (g + a_{tank})] \, dt \qquad (9)$$

is compared to the experimental data for both water and oil. The total dissipated energy in the numerical simulation, $\mathcal{E}_{diss}$, is also reported. In the water case (top plot), apart from an initial discrepancy between $t/T = 1$ and $t/T = 2$, due to the observed differences in the force acting in the initial stage of the experiment, the numerical and experimental curves are parallel each other, providing evidence that the numerical dissipation is close to the experimental one. The final difference is about 6% of the total dissipated energy. For the oil case (bottom plot) the experimental and numerical curves are very close to each other, up to about $t/T = 5$. Then they start to diverge, and at the end of the simulation the relative error is about 16%. For this case the 3D effects are likely to be more important than for the water test case: wall boundary layers develop also on the front and the rear walls which are not modelled in the present 2D simulation. This aspect will be further investigated in future work where 3D simulations will be performed.

B. Test N.2: Sloshing in coupled motion: comparison with the experimental results

Finally, in this section a set of simulations are carried out this time considering the influence of the liquid on the overall motion of the structure, hence analyzing the coupled system for which the tank motion becomes an unknown. Results will be further compared with experiments to report influence of the coupling on the previous results. The considered system

is a 1-DoF system, in the same fashion as is done in the experiments, having the form:

$$F_{slosh} - B_{0d} \cdot \text{sign}\left(\frac{dy}{dt}\right) - B_{1d} \cdot \frac{dy}{dt} - K \cdot y = m_s \frac{d^2 y}{dt^2} \qquad (10)$$

where forces coming from different sources that act on the tank are: F_{slosh} is the contribution from the internal fluid action, $K \cdot y$ corresponds to the restoring force that comes from the springs in this particular configuration (see figure 1) and $B_{0d} \cdot \text{sign}\left(\frac{dy}{dt}\right) - B_{1d} \cdot \frac{dy}{dt}$ is composed by two terms modelling a Coulomb friction and a viscous friction term respectively. Both B_{0d} and B_{1d} are coefficients that can be determined experimentally from a dry test. The values for each of the above coefficients are $m_s = 2.403 kg$, $K = 4321.62 N/m$, $B_{0d} = 0.38 N$ and $B_{1d} = 1.73 kg/s$.

Figure 12 presents the evolution of the tank vertical position for both water (top) and oil (bottom) cases. In both plots, the tank position obtained from the coupled simulations, in which the forces are computed by SPH, is compared to the ones measured in the experiments. As it can be seen, the match between experimental and numerical curves is very close. The numerical curves depicted correspond to the ensemble average computed from a set of 10 repetitions similarly to what is done in section VI-A. The adopted resolution is $N = 200$. Accordingly, variability between the simulations is represented in terms of standard deviation, which is shown in this figure in a lighter color. It is worth noting that the standard deviation increases towards the end of the simulation; this is a consequence of a slight phase shift occurring between the different realizations rather than an actual variation of the motion amplitude. However, from the results in 12 it can be observed that the repeatability is high in terms of tank motion when the full coupled system is taken into account. Two aspects already discussed in the previous section are confirmed
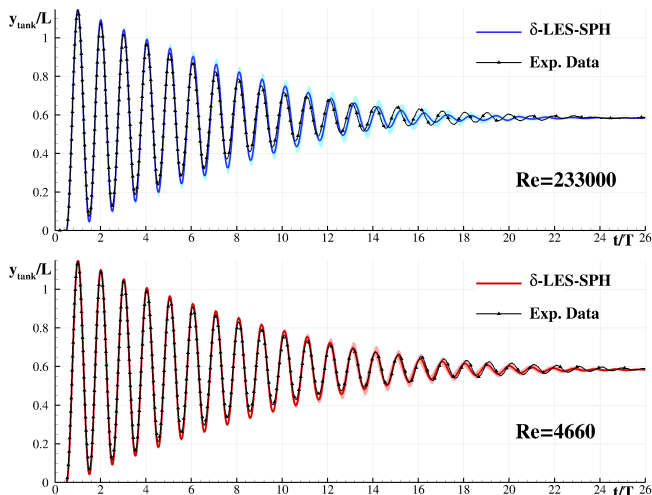
Fig. 12. Evolution of the vertical position of the tank over time obtained from the FSI-SPH simulation at N=200. Top figure corresponds to Re=233,000 for water and bottom figure to Re=4,660 for oil. The experimental signal obtained from the accelerometer is plotted for comparison.

here: i) the 2D SPH simulation predicts a lower dissipation with respect to the experimental case; ii) in the water test case the energy is dissipated more rapidly with respect to the oil case, confirming that in latter case the energy dissipation mechanism is less effective.

VII. Conclusion

The δ-LES SPH formulation is applied to study sloshing flows resulting from violent forced decay heave motions with specific focus on fluid energy dissipation. Despite the simplified physical model of the problem that is used, including a 2D computational domain, single-phase fluid and lack of surface tension forces, the solver is able to obtain accurate results, not only with prescribed movement coming from the records registered from the experiments, but also if the tank is coupled to a mass-spring-damper model. Two different Reynolds regimes corresponding to two different fluids (water and oil) have been tested showing the sensitivity of the numerical simulation to this parameter, not only in terms of convergence but also in terms of simulation repeatability. The liquid impacts have proven to play a major role in the energy dissipation mechanisms. When numerical predictions are compared to experiments, good agreement is obtained in terms of global forces. The agreement is less favourable when the work done by the system is compared to the experimental estimations. However, in the final fully coupled FSI-SPH simulation tank motions time histories are quite close to the ones obtained experimentally. Further, the predicted tank motions are less affected by repeatability issues with respect to the forced motion cases.

Acknowledgments

References

[1] M. Antuono, A. Colagrossi, and S. Marrone. Numerical diffusive terms in weakly-compressible SPH schemes. *Computer Physics Communications*, 183(12):2570–2580, 2012.

[2] M Antuono, S Marrone, A Colagrossi, and B Bouscasse. Energy balance in the δ-SPH scheme. *Computer Methods in Applied Mechanics and Engineering*, 289:209–226, 2015.

[3] M Antuono, S Marrone, A Di Mascio, and A Colagrossi. Smoothed particle hydrodynamics method from a large eddy simulation perspective. generalization to a quasi-lagrangian model. *Physics of Fluids*, 33(1):015102, 2021.

[4] M Antuono, PN Sun, S Marrone, and A Colagrossi. The δ-ALE-SPH model: An arbitrary lagrangian-eulerian framework for the δ-SPH model with particle shifting technique. *Computers & Fluids*, 216:104806, 2021.

[5] XY Cao, L Tao, A-M Zhang, and FR Ming. Smoothed particle hydrodynamics (sph) model for coupled analysis of a damaged ship with internal sloshing in beam seas. *Physics of Fluids*, 31(3):032103, 2019.

[6] J.L. Cercos-Pita, M. Antuono, A. Colagrossi, and A. Souto-Iglesias. SPH energy conservation for fluid–solid interactions. *Computer Methods in Applied Mechanics and Engineering*, 317:771–791, 2017.

[7] A Di Mascio, M Antuono, A Colagrossi, and S Marrone. Smoothed particle hydrodynamics method from a large eddy simulation perspective. *Physics of Fluids*, 29(3):035102, 2017.

[8] M. D Green and J. Peiró. Long duration sph simulations of sloshing in tanks with a low fill ratio and high stretching. *Computers & Fluids*, 174:179–199, 2018.

[9] Y. Green, M.D. Zhou, J.M. Dominguez, M.G. Gesteira, and J. Peiró. Smooth particle hydrodynamics simulations of long-duration violent three-dimensional sloshing in tanks. *Ocean Engineering*, 229:108925, 2021.

[10] A. Khayyer, Y. Shimizu, H. Gotoh, and S. Hattori. Multi-resolution isph-sph for accurate and efficient simulation of hydroelastic fluid-structure interactions in ocean engineering. *Ocean Engineering*, page 108652, 2021.

[11] Pierre Lubin, Stéphane Vincent, Stéphane Abadie, and Jean-Paul Caltagirone. Three-dimensional large eddy simulation of air entrainment under plunging breaking waves. *Coastal engineering*, 53(8):631–655, 2006.

[12] S. Marrone, A. Colagrossi, A. Di Mascio, and D. Le Touzé. Prediction of energy losses in water impacts using incompressible and weakly compressible models. *Journal of Fluids and Structures*, 54:802–822, 2015.

[13] S. Marrone, A. Colagrossi, A. Di Mascio, and D. Le Touzé. Analysis of free-surface flows through energy considerations: Single-phase versus two-phase modeling. *Phys. Rev. E*, 93:053113, May 2016.

[14] J. Martinez-Carrascal and L. M. Gonzalez-Gutierrez. Experimental study of the liquid damping effects on a sdof vertical sloshing tank. *Journal of fluids and structures*, 100, 2021.

[15] Domenico D Meringolo, Salvatore Marrone, Andrea Colagrossi, and Yong Liu. A dynamic δ-sph model: How to get rid of diffusive parameter tuning. *Computers & Fluids*, 179:334–355, 2019.

[16] Stephen B Pope. Ten questions concerning the large-eddy simulation of turbulent flows. *New journal of Physics*, 6(1):35, 2004.

[17] Joseph Smagorinsky. General circulation experiments with the primitive equations: I. the basic experiment. *Monthly weather review*, 91(3):99–164, 1963.

[18] PN Sun, A Colagrossi, S Marrone, M Antuono, and A-M Zhang. A consistent approach to particle shifting in the δ-plus-sph model. *Computer Methods in Applied Mechanics and Engineering*, 348:912–934, 2019.